[American Journal of Science, Vol. 309, June, 2009, P. 450–475, DOI 10.2475/06.2009.02]

EXSOLUTION BY SPINODAL DECOMPOSITION II: PERTHITE FORMATION DURING SLOW COOLING OF ANATEXITES FROM NGORONGHORO, TANZANIA

R. ABART*, E. PETRISHCHEVA*, R. WIRTH**, and D. RHEDE**

ABSTRACT. Perthites in slowly cooled granulite facies rocks from the Ngoronghoro structure (Tanzania) show complex microstructures reflecting several stages of exsolution and coarsening. Mesoperthites with an integrated bulk composition of Or26.5Ab71An2.5 are comprised of lamellar intergrowth of 5 to 10 μm wide orthoclase-rich and albite-rich lamellae. Spindle perthites with a bulk composition of Or67Ab31.5An1.5 are comprised of 2 to 10 μm wide and several 10's of μm long albite-rich spindles in an orthoclase-rich host. In the mesoperthite primary exsolution occurred by spinodal decomposition, whereas the spindle perthite formed by a nucleation and growth mechanism. The interfaces between the exsolved phases are generally incoherent. Unmixing and coarsening of the mesoperthite is discussed in the light of non-linear uphill diffusion. The microstructure evolution and successive chemical separation of the exsolved phases during cooling are modeled based on Cahn-Hilliard theory. We find that coarsening primarily occurs during the first 20 °C to 30 °C of cooling after the homogeneous precursor feldspar has entered the coherent spinodal. The extent of coarsening and the characteristic size of the exsolved phases depend on the cooling rate over this temperature interval. For geologically relevant cooling rates on the order of 5°C/Ma to 50 °C/Ma the compositions of the exsolved phases develop along the solvus down to about 480 °C to 530 °C and are "frozen in" only at lower temperatures. The compositions that are finally preserved in the orthoclase-rich and in the albite-rich phases depend on cooling rate over this temperature interval. Both the characteristic lamella width of the mesoperthite as well as the compositions of the exsolved phases indicate slow cooling at $\leq$ 5 °C/Ma during the coarsening stage and down to about 450 °C. During later stages of the cooling history the albite-rich phase of the mesoperthite exsolved about the peristerite gap, and the orthoclase-rich host of the spindle perthite exsolved a second generation of coherent albite-rich spindles. The incoherent phase boundaries of the primary perthite microstructures served as passageways for fluids during late stage deuteric alteration, which lead to secondary coarsening in the mesoperthite and to alteration of the albite-rich precipitates in the spindle perthite. Finally, both types of perthites were replaced by coarse grained patch perthite during deuteric alteration.

INTRODUCTION

At high temperatures the alkali feldspars form a continuous solid solution between the sodium and potassium end-members, albite ($NaAlSi_3O_8$) and sanidine ($KAlSi_3O_8$). At temperatures below about 600 °C to 800 °C, depending on pressure and the state of Al-Si ordering, a miscibility gap opens (see fig. 1). If a hypersolvus alkali feldspar of intermediary composition is brought into the two phase equilibrium domain by cooling, it tends to exsolve to form perthite, micro- or cryptoperthite, depending on the characteristic dimensions of the exsolved phases (Smith and Brown, 1988). Exsolution may occur by nucleation and growth and/or by spinodal decomposition (Cahn, 1968). Irrespective of the exsolution mechanism, the initial phase separation stage is followed by coarsening. Coarsening may be diffusion controlled and, hence, time and temperature dependent. The coarsening kinetics of micro- and cryptoperthites, which typically are produced during rapid cooling in volcanic and

* Institute of Geological Sciences, Freie Universität Berlin, Malteserstrasse 74-100, D-12249, Berlin, Germany

** Helmholtzzentrum Potsdam, Deutsches GeoForschungsZentrum, Telegraphenberg, D-14473, Potsdam, Germany

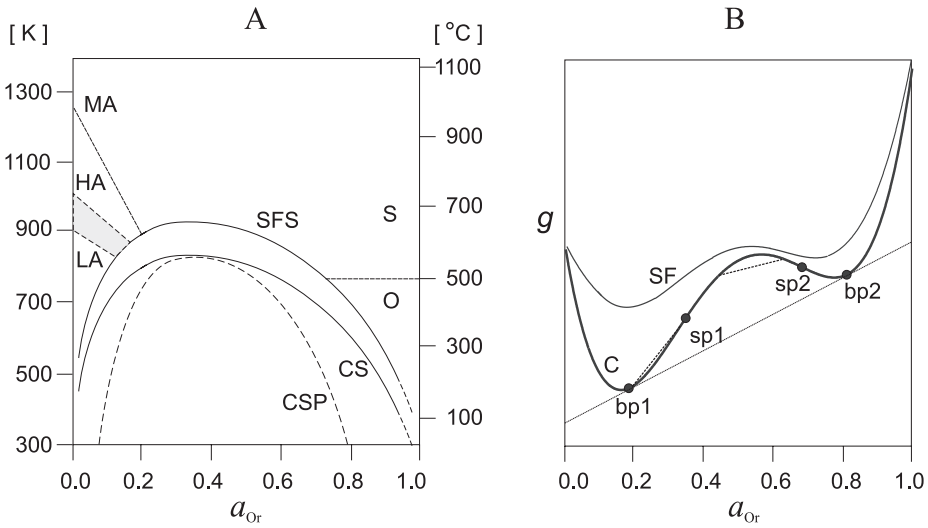

Fig. 1. (A) Shematic $T - a$ phase diagram showing the subsolidus phase relations in the alkali feldspar system, SFS—strain free solvus, CS—coherent solvus, CSP—coherent spinodal curve; also indicated are the phase transformations in albite-rich and in orthoclase-rich alkali feldspar, MA—monalbite, HA—high albite, LA—low albite, S—sanidine, O—orthoclase; (B) schematic $g - a$ diagram; SF—$g - a$ curve for strain free phase relations, C—$g - a$ curve for coherent phase relations; bp1 and bp2—binodal points as defined by the common tangent to the $g - a$ curve, sp1 and sp2—spinodal points. Dashed straight line segments on the $g - a$ curve for coherent phase relations illustrate that the molar Gibbs free energy of a mechanical mixture of chemically separated domains is lower than the Gibbs free energy of the homogeneous phase in the compositional range between sp1 and sp2, where the $g - a$ curve is upwards convex; the opposite is true in the compositional range between bp1 and sp1 and sp2 and bp2, where the $g - a$ curve is convex downwards.

sub-volcanic environments, are understood relatively well (Yund, 1984). The coarsening of exsolved alkali feldspars was calibrated experimentally (Yund, 1974; Yund and Davidson, 1978), and cooling rates were determined from natural cryptoperthites from lava flows (Yund and Chapple, 1980) and from subvolcanic dikes (Christoffersen and Schedl, 1980).

In contrast, the kinetics of exsolution and microstructure evolution in coarse grained perthites are poorly known (Yund, 1984). Exsolution over prolonged periods of thermal annealing or during slow cooling may involve partial or complete loss of coherency and formation of complex microstructures. Coarse perthites with incoherent phase boundaries and with a rich inventory of microstructures have been described from high grade metamorphic rocks and from slowly cooled magmatic rocks (Kay, 1977; Parsons, 1978; Yund and Ackermand, 1979; Yund and others, 1980; Day and Brown, 1980; Parsons and Brown, 1983; Brown and Parsons, 1984, 1988; Parsons and others, 2005; Fitz Gerald and others, 2006). It is not clear in the context of coarse grained perthites how far in time and temperature the experimentally determined coarsening rates can be extrapolated, and whether they are applicable to coarse perthite microstructures at all. Although diffusion is identified as the rate controlling process during exsolution experiments, it is questionable whether this is the prime control on coarsening and chemical evolution of the exsolved phases during slow cooling of natural rocks.

We investigate coarse grained perthites from anatexites of the granulite facies metamorphic Ngoronghoro area, Tanzania. We compare a spindle perthite and a mesoperthite from the same locality, both of which went through several stages of

exsolution and coarsening. We can discern an early perthite generation, which reflects exsolution and primary coarsening of a hypersolvus alkali feldspar at high temperature. This first perthite generation is partially replaced by a coarse patch perthite, which was formed during deuteric alteration. We investigate high temperature exsolution and primary coarsening using a generalization of Cahn-Hilliard theory for anisotropic interface energy. The derivation of the theory and a detailed discussion of the resulting thermodynamic model that can be applied to spinodal decomposition in systems with anisotropic interface energy can be found in part I of this communication (Petrishcheva and Abart, 2009). Although we do not model the sub-solidus phase transformations in alkali feldspar explicitly, the complications that arise from the monoclinic to triclinic transformation and associated Al-Si ordering in the albite-rich phase of the perthites are accounted for in a semi-quantitative way. We further make qualitative statements on secondary coarsening and late stage microstructure evolution, which are primarily based on petrographic observations.

Exsolution in Alkali Feldspar

At temperatures below about 600 °C and low pressure, alkali feldspar of intermediate composition is metastable or unstable with respect to an association of a more sodium-rich and a more potassium-rich feldspar. The corresponding solvus has a relatively shallow limb on the orthoclase-rich side and a steeper limb on the albite-rich side (see fig. 1). If a homogeneous alkali feldspar of intermediate composition is brought into the two phase equilibrium domain during cooling, it will exsolve. Exsolution may occur by either one or a combination of the two kinetic pathways represented by nucleation/growth and spinodal decomposition (Cahn, 1968; Champness and Lorimer, 1976; Brown and Parsons, 1984; Yund, 1984).

Spinodal decomposition of alkali feldspar is effected through substitutional inter diffusion of sodium and potassium cations in the interstices of the aluminosilicate framework, while the aluminum and silicon cations remain in place. As a consequence, the newly formed phase boundaries are coherent with respect to the tetrahedral framework. Due to the difference in ionic radii of Na^+ and K^+, coherency at the phase boundaries implies a distortion of the lattices, which is referred to as the *coherency strain*. The associated elastic strain energy acts against phase separation. This is why the coherent solvus is located at somewhat lower temperature than the strain free solvus (see fig. 1). Phase separation in alkali feldspar is best described by the coherent phase relations, at least during the initial exsolution stage.

Spinodal decomposition may occur, when the originally homogeneous phase is at a condition, where it is unstable with respect to compositional fluctuations (Cahn, 1962, 1968). In a binary system the domain of instability is defined by the inequality

$$\frac{\partial^2 g}{\partial a^2} < 0,$$

where g is the molar Gibbs free energy of the solution phase, and a is a mole fraction (Petrishcheva and Abart, 2009). At given pressure and temperature this is the compositional range, where the respective $g - a$ curve is convex towards high values of g (see fig. 1). In $T - a$ space this domain is bounded by the spinodal curve. Within the spinodal region any compositional fluctuation that produces local chemical separation leads to a decrease in the free energy, and the molar Gibbs free energy of a mechanical mixture of chemically separated domains is lower than that of the homogeneous phase (see straight dashed line between sp1 and sp2 in fig. 1B). There is thus no energy barrier to be overcome for the system to segregate into two phases of different compositions. This is why within the spinodal region compositional fluctuations grow spontaneously and develop towards the binodal compositions. It is important to note

that compositional fluctuations with a specific "wavelength" grow much faster than compositional fluctuations at other wavelengths (Nauman and He, 2001). This leads to a characteristic periodicity in the exsolution microstructure and to a narrow size distribution of the exsolved phases.

The region between the spinodal and binodal curves represents the domain where a homogeneous alkali feldspar is metastable with respect to exsolution (fig. 1). In this domain, small compositional fluctuations lead to an increase in the free energy (see straight dashed line between bp1 and sp1 in fig. 1B). In this case an energy barrier needs to be overcome for a homogeneous alkali feldspar to separate into two phases by a nucleation and growth process.

As there is no nucleation barrier to be overcome during spinodal decomposition, the process is considered to be relatively fast compared to nucleation and growth. There are several lines of evidence suggesting that spinodal decomposition is the prevailing exsolution pathway in rapidly cooled alkali feldspar (Brown and Parsons, 1984; Smith and Brown, 1988) and during isothermal annealing experiments (Yund and Davidson, 1978). Slow cooling favors exsolution by a nucleation/growth mechanism, because a homogeneous feldspar may remain within the field of metastability over long enough time for nucleation to occur.

Coarsening of Perthite Microstructure

The initial exsolution stage is followed by coarsening. We distinguish between primary coarsening, which is driven by the reduction of interfacial energy (Cahn, 1962, 1968; Nauman and He, 2001), and secondary coarsening, which may occur by recrystallization during deuteric alteration.

Irrespective of the exsolution mechanism, the rate of primary coarsening is diffusion controlled and, hence, time and temperature dependent. Exsolution microstructures in alkali feldspar are therefore potential geo-speedometers. This fact motivated experimental investigations into the coarsening of perthite microstructures (Yund and others, 1974; Yund and Davidson, 1978; Hovis and others, 2003). In isothermal anneals, it was generally found that coarsening follows the rate law (Yund and others, 1974; McCallister and Yund, 1977; Yund and Davidson, 1978; Grove, 1982)

$$\lambda = \lambda_0 + kt^{1/3},$$

where λ_0 is the initial wavelength obtained during the exsolution stage, k is a kinetic constant and t is time. The characteristic values of λ_0 and the temperature dependence of the kinetic constant k for exsolution of alkali feldspar were determined by Yund and Davidson (1978). In this rate law, the driving force for phase separation, that is the degree of supersaturation of the homogeneous precursor phase with respect to the exsolved phases, and the kinetic processes including the formation of new phase boundaries and chemical mass transfer by diffusion are integrated into a single kinetic parameter k. As a consequence, this rate law can only describe the evolution of a single observable, that is the characteristic length scale of the exsolution microstructure. It does not, however, describe the evolution of the compositions and the morphologies of the exsolved phases with time.

During the annealing experiments of Yund and Davidson (1978) only the initial stages of coarsening, when the phase boundaries were still coherent, could be covered. The inferred rate law can thus only be applied to crypto– or microperthites with coherent phase boundaries, which are typical for rapidly cooled igneous rocks. The microstructure evolution associated with alkali feldspar exsolution during slow cooling may be complicated by the competition between homogeneous or heterogeneous nucleation and spinodal decomposition. During cooling, the exsolved phases of the perthite are affected to different degrees by symmetry brakes and changes in Al-Si

ordering (Kroll and others, 1980) (see fig. 1A). This may lead to changes in exsolution and coarsening kinetics, which can not be accounted for with a simple rate law with only one kinetic parameter. In our model we explicitly account for interdiffusion of the alkali cations and for the contribution of the newly formed phase boundaries to the bulk free energy of the perthite. This allows the prediction of the evolution of two observable features, namely the microstructure and the compositions of the exsolved phases, which can then be compared to natural or synthetic examples.

GEOLOGICAL BACKGROUND

The feldspars studied are from a ruby bearing anatectic gneiss from the Ngorongoro structure in the Uluguru mountains some 30 kilometers east of the town of Morongo (eastern Tanzania). The Uluguru mountains pertain to the Mozambique belt, a N-S trending orogenic structure at the eastern margin of the Tanzania Craton. Within the Mozambique belt, high pressure granulites, which attained their peak metamorphic conditions at about 650 to 620 Ma, are present over large areas. The Mozambique belt is part of the Pan African mobile belt, which was attributed to the collision between East and West Gondwana (Maboko and others, 1985; Meert and others, 1995). The plate tectonic collision model was modified by Appel and others (1998), who propose a granulite facies stage caused by magmatic underplating and coeval loading of the lower crust some 70 to 100 Ma prior to continental collision.

The peak metamorphic conditions attained during the granulite facies stage are 0.9 to 1.1 MPa and 810 ± 40 °C (Appel and others, 1998). This is consistent with the presence of sillimanite and kyanite in metapelites and with the high pressure granulite assemblage garnet + orthopyroxene + quartz in mafic rocks. According to Appel and others (1998), the prograde evolution started in the kyanite field but mainly developed in the sillimanite field. The retrograde path went through the kyanite field indicating an initial period of slow and close to isobaric cooling prior to tectonic uplift.

The highest-grade microstructures are preserved in meta-anorthosites of the central Uluguru Mountains. Metamorphic textures indicate recrystallization at higher amphibolite-facies down to greenschist-facies conditions. The basal rock unit in the Uluguru mountains is a suite of metaigneous rocks, which includes migmatitic gneisses, granitoid gneisses, enderbites, anorthosites and mafic granulites. Typical mineral assemblages contain Grt + Cpx + Hbl + Pl ± Scp ± Opx ± Qtz ± Bt ± Ep/Czo. The formation of garnet coronas around pyroxene indicates near isobaric cooling following the metamorphic peak (Appel and others, 1998). Spinel coronas followed by a rim of anorthite around corundum in a Cpx-rich mafic to ultramafic granulite document a pressure decrease following the isobaric cooling stage. A pressure decrease is also indicated by the growth of plagioclase + biotite at the expense of garnet in garnet-bearing orthogneisses and metapelites. Lower-T conditions and fluid infiltration during late stages of the metamorphic evolution are represented by muscovite growth and saussuritization of plagioclase.

ANALYTICAL METHODS

Mineral compositions were analyzed on a JEOL JXA-8200 microprobe at Free University Berlin using 15 kV acceleration voltage, 10 nA beam current and a defocused beam. Mineral standards and phi-rho-z correction were applied for quantitative analysis. Element mapping with high spatial resolution was done on a JEOL thermal field emission type electron-microprobe JXA-8500F (HYPERPROBE) at the GFZ Potsdam. Element mapping was done in WDS mode at an acceleration voltage of 8 kV. To minimize migration and loss of sodium forty frames were integrated with 10 ms dwell time per pixel each. A liquid nitrogen trap was used to minimize surface contamination during mapping.

For TEM work, both conventionally ion thinned samples and TEM foils prepared using focused ion beam (FIB) technique were used. TEM foils were prepared at GFZ Potsdam on a FEI TEM200 FIB instrument. Details of the FIB TEM foil preparation are given elsewhere (Wirth, 2004). TEM work was done on a FEI F20 X-Twin instrument at GFZ Potsdam. The TEM is equipped with a Gatan imaging filter GiF Tridiem. EEL spectra were acquired in diffraction mode with an acquisition time of 1 second. Dispersion was 0.1 eV/channel. The GiF entrance aperture diameter was 2 μm. For data evaluation the Digital Micrograph software package was used. EDX analyses were done with an EDAX X-ray detector equipped with an ultrathin window. The TIA software package was used for data evaluation. EDX spectra were usually acquired in scanning transmission mode (STEM), scanning the electron beam in a preselected window thus minimizing mass loss during acquisition of the spectra. The TEM is equipped with a Fishione high angle annular dark field detector for image acquisition in STEM mode.

PERTHITE MICRO STRUCTURE

The samples studied were provided by courtesy from Dr. H. Bank (Ida Oberstein). They stem from ruby bearing anatexites from the Ngoronghoro structure, which are hosted in kyanite bearing garnet-biotite gneisses. The petrography and metamorphic phase relations of these samples were described in detail by Altherr and others (1982), and only a brief summary of the petrography is given here. The exsolved feldspars occur in medium to coarse grained nests together with albite-rich plagioclase, muscovite, phlogopite and corundum. The grain contacts indicate stable coexistence of all these phases. The nests crosscut the foliation of the host gneiss, which contains kyanite or sillimanite, albite-rich plagioclase, minor muscovite, phlogopite, rutile, and baddeleyite. Based on re-integrated bulk composition and on the exsolution microstructure, two types of exsolved feldspar, a mesoperthite (sample TA-76-3) and a spindle perthite (sample TA-76-7) are distinguished.

Mesoperthite

In sample TA-76-3 alkali feldspar is present as mesoperthite with a co-continuous morphology of alternating orthoclase-rich and albite-rich exsolution lamellae (fig. 2A). The albite-rich lamellae have a composition of Or0-1Ab96-97An3-4. The orthoclase-rich phase is Or90Ab10An0. The modal proportions of albite-rich and orthoclase-rich lamellae are 70 volume percent and 30 volume percent, respectively as determined by image analysis of BSE images. The integrated bulk composition of the lamellar mesoperthite was computed from mineral compositions and modal porportions, and it is Or26.5Ab71An2.5. The lamellae show preferred orientation, where the orientation of the lamella traces is compatible with an orientation parallel to ($\bar{6}01$). The lamellae are recognized as the first generation of exsolution features and are referred to as albite-1 and orthoclase-1 lamellae, respectively (see fig. 3). The characteristic spacing of the alternation of albite-1 and orthoclase-1 lamellae is about 10 to 20 micrometers in the most finely spaced portions of the mesoperthites. The interfaces between orthoclase-1 and albite-1 lamellae are curved, and they are smooth on the scale of several micrometers. On this scale they seem to be unrelated to crystal structure. The albite-rich lamellae show abundant cracks, which cross the lamellae at a high angle and terminate at the interfaces with the orthoclase-rich lamellae (see fig. 3C). The cracks may have been generated during cooling due to differences in the thermal expansion of the albite-rich and the orthoclase-rich lamellae (Kroll, 1984). Under high magnification, a very fine lamellar microstructure is identified within the albite-1 lamellae (see fig. 3F). The traces of these sub-micron sized lamellae are oriented approximately perpendicular to the traces of the albite-1 lamellae. From element distribution maps (see fig. 4F) this microstructure is identified as an alternation of pure albite and a

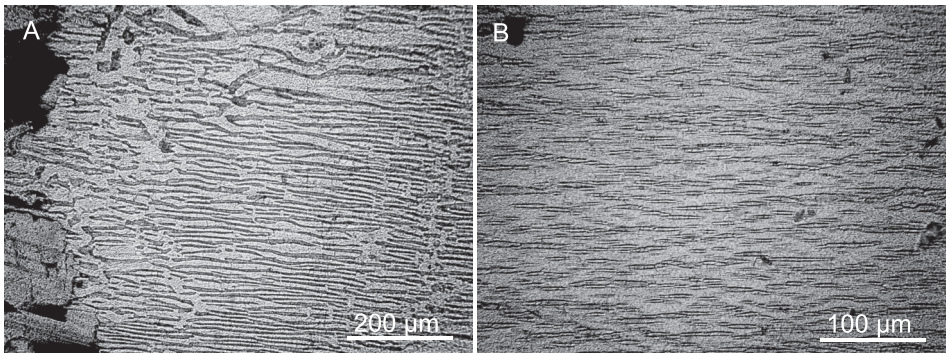

Fig. 2. (A) photo micrograph of mesoperthite from sample Ta-76-3 with co-continuous morphology of albite-rich (dark gray) and orthoclase-rich lamellae (light gray), crossed polarizers; (B) spindle perthite from sample Ta-76-7 with albite-rich spindles in an orthoclase-rich host (crossed polarizers).

plagioclase with some anorthite component. This suggests that albite-1 exsolved about the peristerite gap. It is interesting to note that the interfaces between albite-1 and orthoclase-1 lamellae are corrugated on the sub-micron scale. Lobes of orthoclase-1 extend into the relatively more anorthite-rich lamellae of albite-1 (see fig. 3F), whereas the pure albite lamellae form cusps into the orthoclase.

Within the mesoperthite, a second generation of orthoclase-rich feldspar precipitated, which is henceforth referred to as orthoclase-3. The orthoclase-3 precipitates are irregularly shaped and up to 200 μm in size (see fig. 3B). They host very thin ($<$ 150 nm) albite-rich spindles (see fig. 4E), which clearly distinguish them from the albite-1 lamellae from the primary exsolution. The albite-rich spindles are perfectly straight on the scale of several micrometers, and they have the same orientation as orthoclase-1 lamellae. They are labeled albite-4 in figure 3D. The albite-4 spindles terminate at the contacts between patches of orthoclase-3 and orthoclase-1 lamellae (see fig. 4E). In many cases precipitation of patchy orthoclase-3 leads to coalescence of the pre-existing orthoclase-1 lamellae (see fig. 3D). Through this, the original lamellar microstructure of the mesoperthite is partially obliterated and a coarser and rather irregular microstructure is generated. This is why we refer to this phenomenon as "secondary coarsening".

The lamellar mesoperthite is partially replaced by patch perthite (see fig. 3A). The patch perthite is comprised of an aggregate of patchy precipitates of potassium-rich feldspar embedded in a matrix of albite-rich feldspar. The characteristic size of the precipitates is about 200 μm. The potassium-rich precipitates host very fine ($<$ 150 nm) spindles of albite-rich feldspar (see fig. 3E). Based on the similarities in shape and exsolution features the phases of the patch perthite are inferred to be co-genetic to the phases of secondary coarsening within the mesoperthite. The constituent phases of the patch perthite are hence referred to as albite-3 and orthoclase-3, respectively. The exsolved albite spindles in orthoclase-3 are referred to as albite-4, accordingly. Replacement of the lamellar perthite by the patch perthite occurs at a sharp reaction front. From the geometry of the replacement front it seems that the orthoclase-rich lamellae of the perthite are more easily dissolved than the albite-rich lamellae (see fig. 3C).

Spindle Perthite

In sample TA-76-7 the perthite microstructure is represented by spindle and lath shaped exsolutions of an albite-rich phase in a matrix of orthoclase-rich alkali feldspar (see fig. 2B). This microstructure is identified as the first generation of exsolution features in the spindle perthite. The albite-rich spindles and the orthoclase-rich host

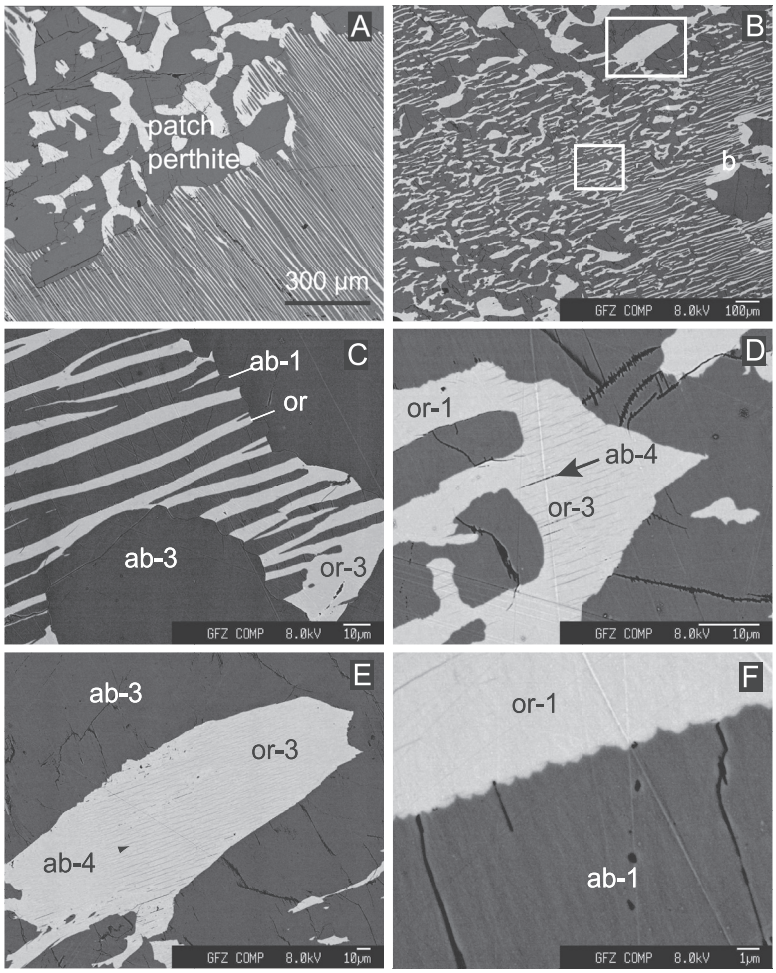

Fig. 3. (A) Back scattered electron image of a mesoperthite-patch perthite assemblage from sample Ta-76-3; the mesoperthite with regular lamellar intergrowth of albite-1 (dark gray) and orthoclase-1 (light gray) lamellae is replaced by patch perthite with irregular intergrowth of albite-3 and orthoclase-3; (B) mesoperthite with secondary coarsening and loss of lamellar microstructure, upper and lower inset indicate positions of the detail images shown in (D) and (E); (C) detail of the lamellar mesoperthite and of the interface to the patch perthite; note the embayment of the replacement front where it meets orthoclase-1 lamellae, the albite-1 lamellae show abundant cracks in the direction approximately perpendicular to the extension of the lamellae, which end at the interfaces to the orthoclase-1 lamellae; (D) detail of secondary coarsening within the mesoperthite, the newly formed orthoclase-3 contains a second generation of albite-rich exsolution lamellae of about 100 to 150 nm width labeled albite-4; (E) orthoclase-3 of the patch perthite with a second generation of fine albite-4 lamellae; (F) detail of albite-1-orthoclase-1 interface within the mesoperthite, note that albite-1 is comprised of an alternation of sub-micron wide lamellae, which are oriented approximately perpendicular to the albite-1 lamella and which have slightly different back scattering intensity, that is anorthite content; the albite-1-orthoclase-1 interface is corrugated on the sub-micron scale; lobes of orthoclase extend into the more anorthite rich lamellae of albite-1.

are hence referred to as albite-1 spindles and orthoclase-1 host, respectively. The albite-1 spindles are evenly distributed and optically continuous under crossed polarizers over the entire host grain. The composition of the albite-1 spindles is Or0-1Ab89-90An5-7, and the composition of the orthoclase-1 host is Or90Ab10An0. The albite-rich spindles constitute about 25 percent of the volume of the exsolved feldspar grains.

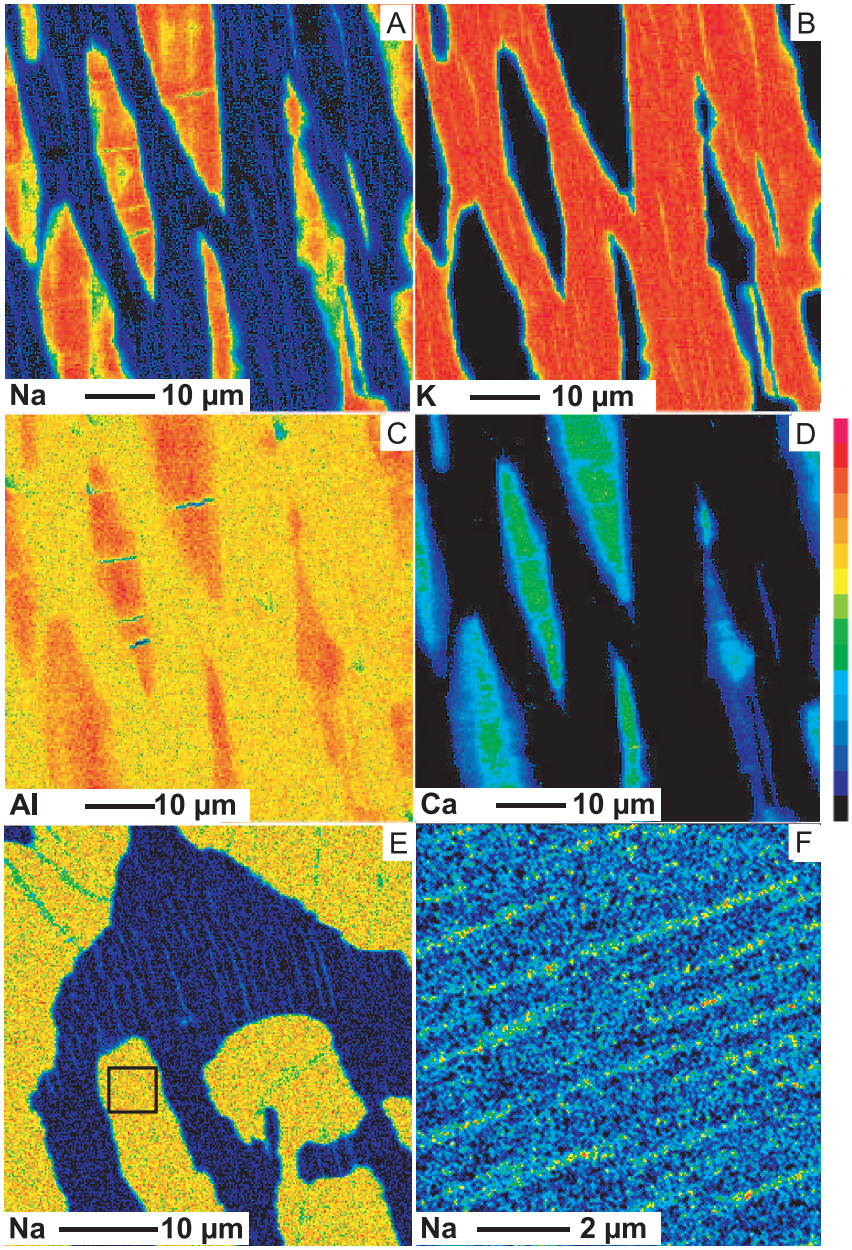

Fig. 4. (A) through (D): element distribution maps of spindle perthite from sample Ta-76-7, (E) and (F) element distribution maps of mesoperthite from sample Ta-76-3, the color code indicates relative signal intensity; (A) fine Na-rich spindles within the orthoclase-rich matrix are identified as albite-2 exsolutions; (C) the aluminum concentration is elevated within albite-1 spindles due to their anorthite content; (D) albite-1 spindles are zoned with respect to their anorthite content; (E) Na distribution in mesoperthite, orthoclase-1 lamellae (lower part) and orthoclase-3 precipitate from deuteric alteration (central portion of the image) surrounded by albite-1; thin sub-vertically oriented spindles with elevated Na content within orthoclase-3 are albite-4 lamellae, rectangle indicates position of detailed Na-distribution map of albite-1 shown in figure (F); (F) spindle shaped exsolution of albite-rich phase within albite-1-peristerite gap.

The integrated bulk composition of the spindle perthite is Or67Ab31.5An1.5. The albite-rich spindles are about 5 to 10 micrometers wide and up to 100 micrometers long and show strong shape preferred orientation (see fig. 5A). Mostly the interfaces between the orthoclase-1 host and the albite-1 precipitates are curved. Only in places they are perfectly straight in two directions and seem to be crystallographically controlled (see fig. 5A). The albite-1 spindles show sub-microscopic albite twinning (see fig. 6A). Figures 4A–D shows element distribution maps of the spindle perthite. Calcium and aluminum are preferentially fractionated into the albite-1 spindles. The spindles are zoned with respect to their calcium content with highest concentrations in the center and an about one to two μm wide albite-rich zone in the outer portion of the spindles (see fig. 4D). Quantitative electron microprobe analysis yield an anorthite content of about 7 to 9 mole percent in the central portion of thick spindles. EDX analysis on an about 100 nanometers thick TEM foil revealed that the calcium concentration in the center of the spindle is higher by a factor of about 3.5 compared to the rims. The transition between the relatively anorthite-rich cores and the anorthite-poor rims is sharp at the scale of less than about 100 nm. The albite-rich rims around albite-1 spindles are interpreted as a replacement or as an overgrowth, which is probably related to late stage fluid infiltration. This interpretation is corroborated by the fact that plagioclase grains in the immediate vicinity of the perthite show similar albite-rich overgrowth (see fig. 5B). In analogy to the phases that are ascribed to deuteric alteration in the mesoperthite of sample TA-76-3, the albite-rich plagioclase overgrowth on albite-1 lamellae is referred to as albite-3. The interfaces between albite-1 spindles and the orthoclase-1 host and between the albite-3 overgrowth and the orthoclase-1 host are never coherent. They are characterized by the presence of a 50 to 200 nm wide zone of extremely fine grained aggregates comprised of albite-rich feldspar (see fig. 6B). This zone also contains abundant pores up to several 100 nm in size (see fig. 6C).

Where the tips of two spindle shaped albite-1 precipitates come close, undulatory extinction is observed in the orthoclase matrix under crossed polarizers. This is probably due to lattice strain, which is concentrated around the tips of the albite-1 spindles. This strain may either be a primary feature, which was generated during exsolution of albite-1 spindles or, alternatively, it may be due to elastic strain that was

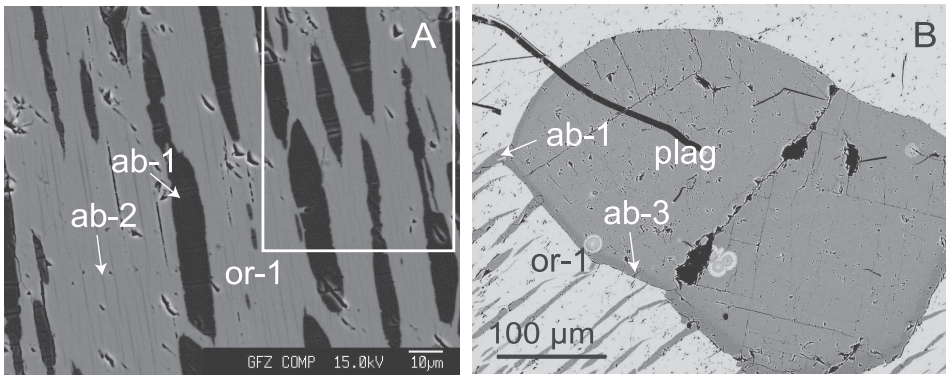

Fig. 5. (A) Back scattered electron image of spindle perthite from sample Ta-76-7; a first generation of exsolved spindles of albite-rich feldspar (albite-1) is immersed in an orthoclase-rich host (orthoclase-1); note the second generation of albite-rich exsolution lamellae (albite-2), with characteristic width of 200 to 400 nanometers within the orthoclase-1 matrix; white rectangle indicates the area for which element distribution maps are shown in figure 4; (B) plagioclase grain (plag) enclosed in a spindle perthite, note the thin rim of more albite-rich plagioclase around plagioclase (albite-3).

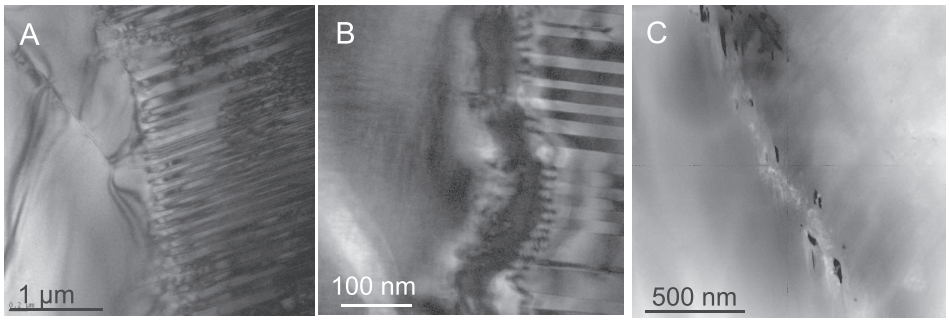

Fig. 6. (A) TEM bright field image of albite-1 spindle from sample Ta-76-7 (spindle perthite) in contact with the orthoclase-1 host; the albite-1 spindle is twinned after the albite law; (B) TEM bright field image of the spindle-host interface of the same sample; an about 50 nm wide zone is developed between the spindle and the host, which does not show the twinning nor does it show the contrast of the orthoclase-rich host; this is supposedly a re-crystallized domain along the spindle-host interface with newly formed albite-rich feldspar grains; (C) high angle annular dark field image (HAADF) showing that 10 to 50 nm wide and up to several 100 nm long holes formed at the spindle-host interface.

attained during cooling because of the different thermal expansion coefficients of albite and orthoclase.

In the back scattered electron image of figure 5C a second generation of spindle shaped albite-rich exsolution features can be discerned in the orthoclase-1 matrix. The spindles are only about 200 to 400 nanometers wide and up to several tens of micrometers long. At contacts between perthite and matrix plagioclase these spindles are truncated by albite-3 overgrowth suggesting that they predate the deuteric alteration. They are hence referred to as albite-2 lamellae. Figure 7A shows a bright field image of a 150 nanometer wide albite-2 spindle. Linear features, which cross the spindle at a high angle and with regular spacing, are interpreted as line defects at the spindle-host interface. Figure 7C shows the corresponding high resolution image. The lattice fringes run across the interface between the albite-2 spindles and the orthoclase-1 host without or with only minor distortion testifying to the largely coherent nature of this interface. The albite-2 spindles occur at a spacing of about 2 μm. Their modal proportion within orthoclase-1 is in the range of 5 to 10 percent.

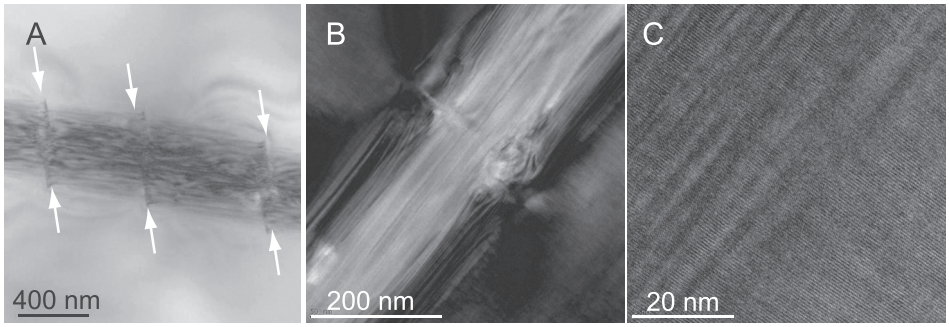

Fig. 7. (A) and (B) TEM bright field images of albite-2 exsolution lamella within the orthoclase-1 host of sample Ta-76-7 (spindle perthite); the linear features crosscutting the lamella in regular intervals (white arrows) are interpreted as line defects at the lamella-host interface; note that albite-2 lamellae are devoid of twinning; (C) high resolution TEM image of the lattice fringes at the interface between albite-2 lamella and orthoclase-1 host; lattice fringes are largely undisturbed at this interface indicating the coherent character of the phase boundary.

It is interesting to note that in the albite-3 overgrowth on albite-1 lamellae, the presence of water can be identified from an OH related pre-peak prior to the onset of the O-K edge in the EEL spectrum (see fig. 8). This pre-peak quickly disappears into the albite-1 lamellae and into the orthoclase-1 host. Also in the albite-2 lamellae there is no sign of water in the EEL spectrum suggesting that the coherent interfaces between albite-2 spindles and the orthoclase-1 matrix did not allow for fluid penetration.

MECHANISMS OF PERTHITE FORMATION

A feature that is characteristic of both the lamellar perthite of sample TA-76-3 and the spindle perthite of sample TA-76-7, is the homogeneous distribution of exsolution phases with relatively uniform grain size and spacing in the entire grain of the

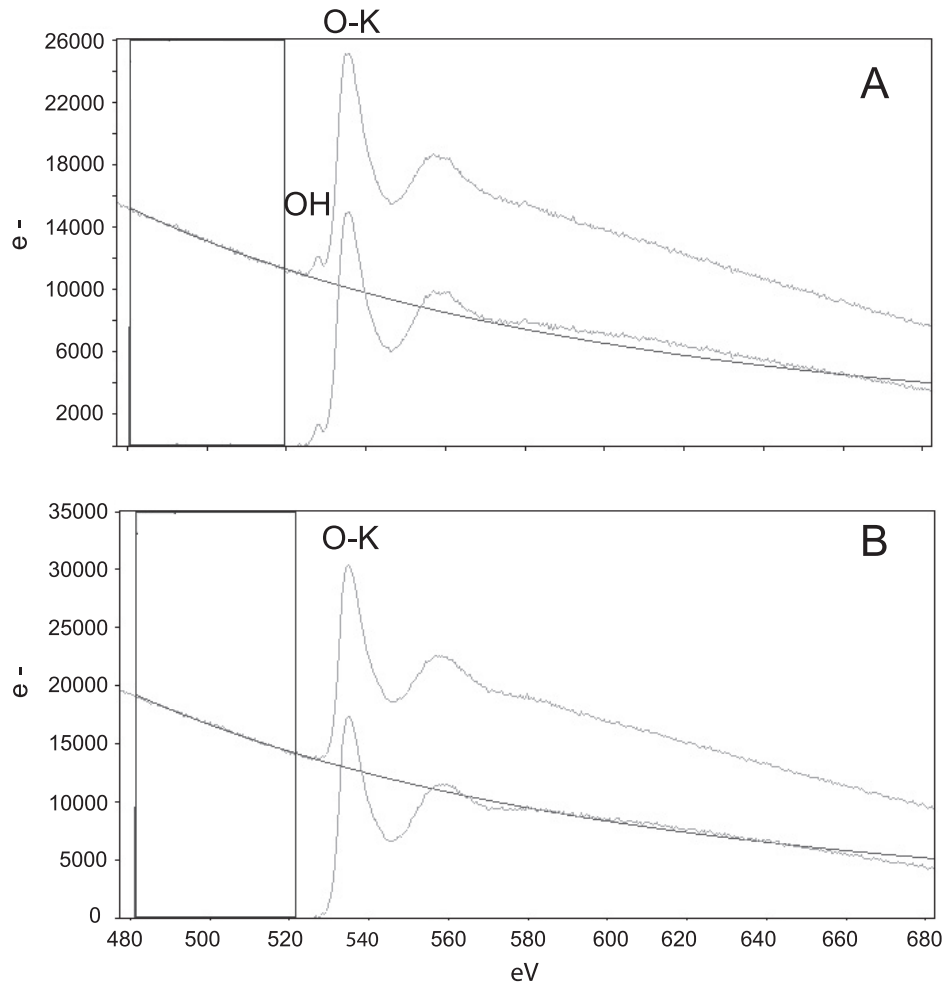

Fig. 8. Electron energy loss spectra (EELS) from albite-1 (A) and albite-2 (B) lamellae in sample Ta-76-7 (spindle perthite); the pre-peak prior to the onset of the O-K edge at about 530 eV in the EELS spectrum (A) indicates that water is present as hydroxyle groups at appreciable concentrations along the incoherent phase boundaries of the albite-1 lamellae, in contrast, such a pre-peak is absent in spectrum (B) indicating that albite-2 lamellae are "dry".

presumably homogenous precursor grain (fig. 2). Although slow cooling favors homogeneous nucleation, spinodal decomposition is still the most likely exsolution mechanism for bulk compositions in the range of 25 to 45 mole percent orthoclase component. This is because an originally homogeneous alkali feldspar of such a composition remains in the field of metastability only over a short temperature and time interval along its cooling path. The perthite from sample TA-76-3 falls into this composition range, and we assume that it indeed exsolved by a spinodal process.

In contrast, for bulk compositions with orthoclase contents higher than 45 mole percent and lower than about 25 mole percent initially homogeneous alkali feldspar remains within the region of metastability between the binodal and spinodal curves over a wider temperature and time interval, favoring exsolution by homogeneous nucleation. Exsolution by homogeneous nucleation is what is anticipated for the perthite from sample TA-76-7.

In the following we develop a model for alkali feldspar exsolution by a spinodal process. Modeling is focused on the microstructure evolution in the mesoperthite.

A thermodynamic model of perthite formation

We employ Cahn-Hilliard theory (Cahn, 1968; Hilliard, 1970) to model unmixing by spinodal decomposition and subsequent coarsening. Herein the system evolution is described by means of a non-linear diffusion equation. This equation is based on a nonlocal free energy functional, which accounts for the notion that, at given pressure and temperature, the local free energy density depends on both composition and compositional gradients (Cahn and Hilliard, 1958). For an isotropic binary system

$$\mathfrak{g}(a, \nabla a) = g(a) + \frac{1}{2}\kappa(\nabla a)^2 \tag{1}$$

where $g(a)$ is the "standard" part of the free energy density as a function of mole fraction a. The second term in equation (1) is referred to as the "gradient energy term". It represents the free energy associated with compositional gradients. Compositional gradients are generally present at phase boundaries, and the gradient energy term accounts for the contribution of interfacial energy to the global free energy in a heterogeneous system. The parameter κ in the gradient energy term is a measure of the interface free energy. A simple non-isotropic generalization of the gradient energy term has been derived in part I of this communication (Petrishcheva and Abart, 2009). It may be written as

$$\frac{1}{2}\kappa(\nabla a)^2 \rightarrow \frac{1}{2}\sum_{ij}\kappa_{ij}\partial_i a \partial_j a.$$

The symmetric second-order tensor κ_{ij} describes the anisotropy of interfacial energy.

The chemical potential of a component in a heterogeneous system is then defined as the variational derivative of the corresponding global free energy functional with respect to the number of moles of the respective component (Nauman and He, 2001). For the general case of anisotropic interfacial energy the continuity equation for diffusion reads (Petrishcheva and Abart, 2009)

$$\partial_t a = \nabla\left[\frac{D}{kT}a(1-a)\nabla\left(\frac{\partial g}{\partial a} - \kappa_{ij}\partial_i\partial_j a\right)\right], \tag{2}$$

where summation over two dummy indices is implied. In the isotropic case $\kappa_{ij}\partial_i\partial_j a$ is replaced by $\kappa\nabla^2 a$, and the classical Cahn-Hilliard equation is obtained. The combination

$$\frac{D}{kT}\, a(1-a)\, \frac{\partial^2 g}{\partial a^2}$$

may be interpreted as an "effective" diffusion coefficient. D is the ideal part of the interdiffusion coefficient and k is the Boltzmann constant. If the $g - a$ surface is concave upwards, that is, $\partial^2 g/\partial a^2 > 0$, the effective diffusion coefficient is positive and diffusion of a chemical component is down its concentration gradient. In this case diffusion leads to a degradation of compositional gradients, and it tends to make the composition of the system uniform. If the $g - a$ surface is convex upwards, that is $\partial^2 g/\partial a^2 < 0$, the effective diffusion coefficient is negative, and the diffusion of a chemical component is uphill with respect to its concentration gradient. The condition $\partial^2 g/\partial a^2 < 0$ defines the spinodal region, where any compositional fluctuation grows spontaneously and an originally homogenous solution phase unmixes.

For a numerical solution of the Cahn-Hilliard equation (2) it is useful to introduce normalized variables

$$\bar{x}, \bar{y}, \bar{z} = \frac{x}{l}, \frac{y}{l}, \frac{z}{l}, \quad \bar{t} = \frac{t}{\tau}, \quad \bar{g}(a) = \frac{g(a)}{kT}, \quad \bar{\kappa}_{ij} = \frac{1}{l^2}\frac{\kappa_{ij}}{kT}$$

and to rewrite the basic equation (2) as

$$\frac{\partial a}{\partial \bar{t}} = \frac{D\tau}{l^2}\, \bar{\nabla}\left[a(1-a)\bar{\nabla}\left(\frac{\partial \bar{g}}{\partial a} - \bar{\kappa}_{ij}\frac{\partial^2 a}{\partial \bar{x}_i \partial \bar{x}_j}\right)\right], \tag{3}$$

where $\bar{\nabla} = (\partial/\partial\bar{x}, \partial/\partial\bar{y}, \partial/\partial\bar{z})$. When the parameters D and κ_{ij} are constant during exsolution one may simplify equation (3) by a suitable choice of l and τ. For instance, in the isotropic case one may set

$$\bar{D} = \frac{D\tau}{l^2} = 1 \quad \text{and} \quad \bar{\kappa} = \frac{1}{l^2}\frac{\kappa}{kT} = 1,$$

so that after normalization the isotropic Cahn-Hilliard equation does not contain any parameters. We are, however, interested in a more complex situation: spinodal decomposition during continuous cooling. In this case $T = T(t)$ and the diffusion coefficient implicitly depends on time

$$D(t) = D_\infty \exp\left(-\frac{E}{kT(t)}\right) \tag{4}$$

with E being the activation energy. In what follows we assume that the value $\kappa_{ij}/(kT)$ is constant over the temperature range of interest (see next section). In the isotropic case we will take $\bar{\kappa} = 1$, in the anisotropic case $\bar{\kappa}_{11} = 1$, so that the value of l is uniquely defined. The Cahn-Hilliard equations (3) and (4) are then solved using

$$\frac{D(t)}{D(0)} = \exp\left(\frac{E}{kT(0)} - \frac{E}{kT(t)}\right),$$

so that

$$\bar{D} = \frac{\tau D(0)}{l^2}\exp\left(\frac{E}{kT(0)} - \frac{E}{kT(t)}\right).$$

The value of τ is chosen in accord with the cooling rate.

MODEL PARAMETERIZATION

As mentioned above, with a suitable normalization one can remove D and κ from the basic equation (2) and carry out numerical modeling with only knowledge of $g\,(a)$. Nevertheless, kinetic and interfacial energy parameters are important for comparison of simulation results and experimental data. The free energy $g\,(a)$, interfacial energy and the kinetic parameters are quantified in this section.

Free Energy of Alkali Feldspar Solid-Solution

The thermodynamic properties of the system are a first order control on its evolution. At given pressure and temperature the free energy of a binary solid solution A-B reads

$$g(a) = [\mu_A^0 a + \mu_B^0(1 - a) + kT(a \ln a + (1 - a)\ln(1 - a)) + g^{ex}],$$

where a is a mole fraction and μ_A^0 and μ_B^0 are the chemical potentials of the pure end-member phase components. They do not contribute to the $g''(a)$ and can be ignored in diffusion modeling. The last two terms account for the configurational contribution to the free energy and for the non-ideality of the solid solution, respectively. We employ the mixing model of Hovis and others (1991), where

$$g^{ex}(a, P, T) = [aW_A(P, T) + (1 - a)W_B(P, T)]a(1 - a)$$

with

$$W_A(P, T) = 22820 - 6.3T + 0.461P$$
$$W_B(P, T) = 19550 - 10.5T + 0.327P\ ,$$

where W is in Joules T is in °K and P is in bar. The strain free solvus predicted from this mixing model for a pressure of 800 MPa is shown as a heavy solid line in figure 9. The strain free solvus closes at about 790 °C at a composition of $a_{or} \approx 0.65$.

Coherency Strain Energy

Due to the considerable difference in ionic radii of Na^+ and K^+, coherent intergrowth of albite- and orthoclase-rich alkali feldspars leads to "coherency strain" (Robin, 1974; Yund and Tullis, 1983). Provided the elastic strain is homogeneous in a coherent lamellar intergrowth of the exsolved phases, the associated strain energy density may be written as (Cahn, 1962)

$$E_{elast} = \frac{\eta^2 E}{1 - \nu}(c - \bar{a})^2 \qquad (5)$$

where η is the linear expansion per unit composition change (compositional strain), E is Youngs modulus, and ν is the Poisson ratio; $\bar{a}$ is the average composition. Robin (1974) demonstrated that the commonly observed orientation of exsolution lamellae in alkali feldspar, which is close to $(\bar{6}01)$, minimizes the coherency strain energy.

The contribution of the coherency strain energy must be accounted for in the free energy function (Cahn, 1962; Robin, 1974; Yund and Tullis, 1983). Note that the elastic strain energy is a quadratic form of the compositional strain. It is always positive and reduces the thermodynamic driving force for phase separation. The sub-solidus equilibrium phase relations in the $KAlSi_3O_8$–$NaAlSi_3O_8$ system that were used for numerical modeling were calculated for disordered alkali feldspar at a pressure of 800 MPa (fig. 9). The coherent phase relations are based on a coherency strain energy calculated after Robin (1974). As long as during coarsening the lamellae remain coherent with homogeneous elastic strain, the elastic strain energy remains un-

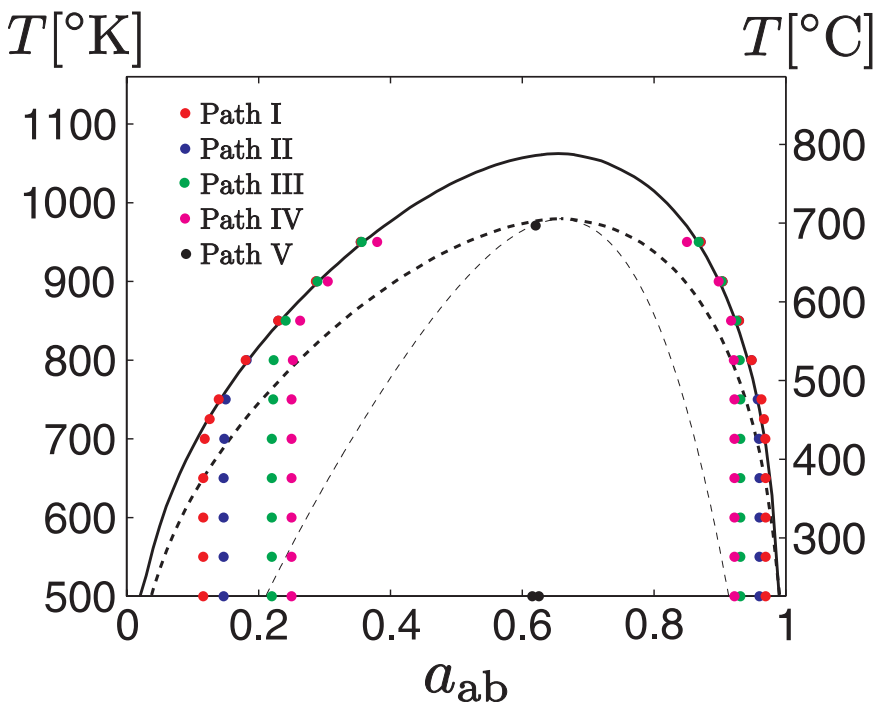

Fig. 9. Strain free solvus (solid line) and coherent solvus and spinodal curves (dashed lines) for alkali feldspar; the strain free phase relations were calculated using the mixing model of Hovis and others (1991); for calculation of the coherent phase relations the contribution of elastic strain energy was considered using the method of Robin (1974); cooling path for alkali feldspar of intermediate composition $a_{ab} = 0.6$ for different cooling rates; path I: 5 °C/Ma, path II: 500 °C/Ma, path III: 0.05 °C/a, path IV: 0.5 °C/a, path V: 1 °C/day.

changed and the compositional relations of the lamellae continue to be defined by the coherent solvus.

The coherent solvus and spinodal are shifted to lower temperatures by about 90 °C with respect to the corresponding strain free solvus. They are shown in figure 9 as heavy and light dashed lines, respectively. The coherent solvus closes at about 690 °C at a composition of $a_{or} \approx 0.65$.

The Gradient Energy Term

The initial wavelength λ_0 that develops during exsolution determines the gradient energy term. For exsolution at constant temperature one may write (Nauman and He, 2001)

$$\lambda_0 = 2\pi \sqrt{-\frac{2\kappa}{g''(a_0)}} = 2\pi \sqrt{\frac{2\kappa/(kT)}{-\bar{g}''(a_0)}}, \qquad (6)$$

where a_0 is the composition of the homogeneous precursor phase. Clearly λ_0 strongly depends on temperature near the bifurcation point where $g'' \approx 0$. Far from the bifurcation point $g'' \sim -1$ and the possible dependence of κ on T may become important. In principle κ can be obtained from the thermodynamics of the alkali feldspar solid solution. Shimizu and Takei (2005) derive κ from the interaction parameters of a regular solution model of metallic systems. For the alkali feldspars this approach yields unrealistically small values for λ_0. This is why we rely on experimentally

produced microstructures to obtain an estimate for λ_0. In isothermal annealing experiments λ_0 was repeatedly found to be in the range of 5 to 15 nm. In principle, the κ parameter can be extracted from the measurement of the initial wavelength of exsolution if both the system temperature and the function $g(a,P,T)$ are known. The existing data are, however, rather contradictory and only a rough estimate of κ can be made; in particular, its dependence on temperature cannot be revealed. For example Yund and Davidson (1978) do not find a systematic dependence of λ_0 on annealing temperature. In contrast, Owen and McConnell (1974) report on a systematic increase of the initial wavelength with increasing annealing temperature from 9 nm at 420°C to 16 nm at 540 °C. Therefore, to keep our model simple, the ratio $l^2 = \kappa/(kT)$ is treated as being constant.

If exsolution takes place during cooling, the relation between the gradient energy term and λ_0 can no longer be described by equation (6). In this case λ_0 depends on the cooling rate s, where the dependence is weak with $\lambda_0 \propto (1/s)^{1/6}$ (Hilliard, 1970). For an alkali feldspar with $a_{or} \approx 0.38$ cooled at a rate of 1 °C/day Yund and Davidson (1978) obtained $\lambda_0 = 7.5$ nm. For geologically reasonable cooling rates of 5 and 50 °C/Ma this yields $\lambda_0 = 153$ nm and 71 nm, respectively. In our modeling, $\kappa/(kT)$ is chosen arbitrarily so as to reproduce the characteristic size of the exsolution microstructure. It is important to note that in our model $\kappa/(kT)$ merely enters into the scaling of length and only has an approximate physical meaning.

The Interdiffusion Coefficient

If perthites form in the pure $NaAlSi_3O_8$–$KAlSi_3O_8$ system, then the relevant kinetic parameter for scaling the time variable is the "ideal" part of the coefficient that describes the substitutional inter-diffusion of sodium and potassium ions in the otherwise fixed tetrahedral framework of an alkali feldspar solid solution. The ideal part of the Na–K interdiffusion coefficient is obtained from the respective tracer diffusion coefficients (Brady, 1983)

$$D = \frac{D^*_K(a_{\mathrm{or}})D^*_{Na}(a_{\mathrm{or}})}{a_{\mathrm{ab}}D^*_{Na}(a_{\mathrm{or}}) + a_{\mathrm{or}}D^*_K(a_{\mathrm{or}})} \tag{7}$$

where a_{or} and a_{ab} are the mole fractions of the respective phase components and $D^*_K(a_{\mathrm{or}})$ and $D^*_{Na}(a_{\mathrm{or}})$ are the tracer diffusion coefficients of sodium and potassium at the specified compositions. The data for Na and K tracer diffusion are taken from Foland (1974) for orthoclase and from Kasper (ms, 1975) for albite.

MODELING RESULTS

Figure 9 shows several paths that an alkali feldspar of intermediate composition may take through the $T - a$ space, when it is cooled at a pressure of 0.8 GPa from 700 °C, that is from a temperature slightly above the coherent solvus, down to 227 °C, that is into the two phase equilibrium domain. We consider five different cooling rates, where cooling rates are taken to be constant with time. For a given value of $l^2 = \kappa/(kT)$, the cooling rates for paths I, II and III differ by a factor of 100 so that $s^{III} = 100s^{II} = 10000s^{I}$. The cooling rate for path IV is by a factor of 10 larger than the cooling rate for path III. For comparison also the evolution during cooling at 1K/day is given in path V, which is representative for volcanic production. We choose $\kappa/(kT)$ so that we obtain exsolution lamellae of several μm width from our numerical simulation. Considering that depending on cooling rate we observe an increase of the characteristic size of the exsolution lamellae by a factor of 2 to 7 in our modeling, this translates to an initial wavelength on the order of 0.1 to 1 μm. This is of the same order of magnitude as λ_0 obtained from extrapolation of the experimental data of Yund and Davidson (1978). For this choice of $\kappa/(kT)$ cooling paths I and II represent cooling

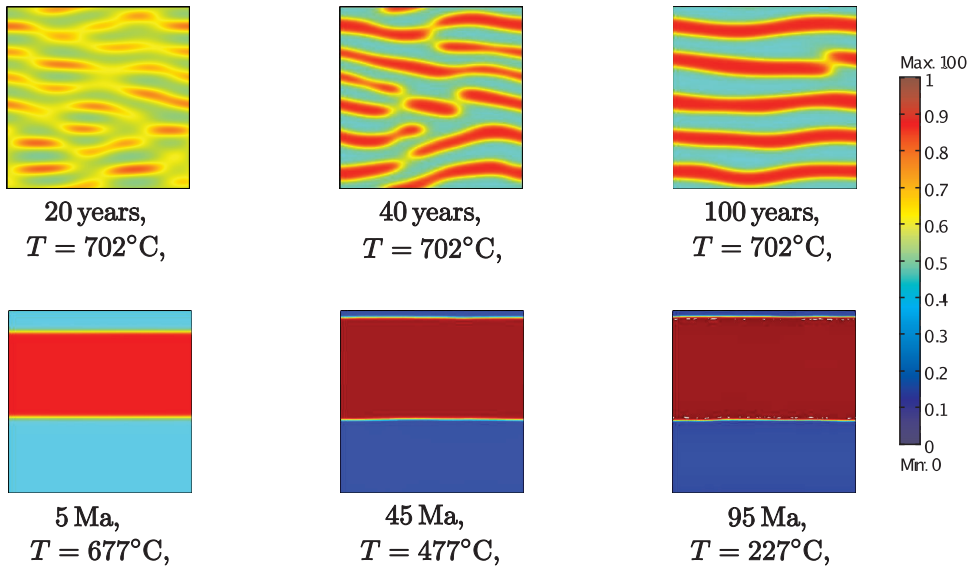

Fig. 10. Microstructure evolution of an alkali feldspar of composition $a_{ab} = 0.62$ for a cooling rate of 5 °C/Ma. Images show $a - b$ sections through the monoclinic alkali feldspar.

rates of 5 and 500 °C/Ma, respectively. This covers the range of cooling rates that may be expected for regional metamorphism. Paths III and IV represent cooling rates of 50,000 °C/Ma (0.05 °C/a) and 500,000 °C/Ma (0.5 °C/a), which may be representative for cooling around small and shallow intrusions.

During the initial separation stage, the exsolution microstructure was probably coherent, and the shape anisotropy and shape preferred orientation of the exsolved phases was most likely dictated by the minimization of coherency strain (Robin, 1974). The phase boundaries of primary exsolution microstructures examined in the perthites from Ngoronghoro are, however, all incoherent. It is, hence, assumed in our modeling that the phase boundaries lost coherency during the coarsening stage. As a consequence, the compositions of the separated phases develop along the strain free solvus in our model. The observed shape anisotropy of the exsolved phases in the perthites from Ngoronghoro was either inherited from an early stage of exsolution, when the microstructure was still coherent, or, alternatively, it may result from the anisotropy of diffusion (Kuhl and Schmid, 2007) and/or from the anisotropy of the interfacial energy (Petrishcheva and Abart, 2009). In our modeling, we consider the latter possibility. The microstructures corresponding to different stages of cooling path I are shown in figure 10. The patterns shown represent sections parallel to the $a - b$ plane of the monoclinic alkali feldspar. They were calculated considering an anisotropy in interfacial energy of $\kappa_{11}/\kappa_{22} = 4$.

As there is no nucleation barrier to be overcome, phase separation by spinodal decomposition is considered to proceed rapidly. This is well reflected by our modeling. Only for the extremely rapid cooling of cooling path V, chemical separation is inefficient. Actually, chemical separation does take place, albeit with a very low amplitude. Such behavior was reported from sanidine contained in ejecta from the Stromboli volcano (Menna and others, 2008).

Chemical separation is much more efficient during slow cooling. During the slow cooling of paths I to IV chemical separation produces compositions that closely approach the strain free solvus after cooling by a few degrees below the coherent

solvus, that is after a very short time. During subsequent cooling the exsolved phases successively equilibrate along the solvus to lower temperatures and become increasingly more chemically separated.

At some point along the cooling path, the compositions of the exsolved phases begin to depart from the solvus and eventually become "frozen in". The temperature at which the compositions of the exsolved phases depart from the solvus and the compositions that are finally preserved in the albite-rich and in the orthoclase-rich phase of the perthite depend on the cooling rate. For cooling paths I and II the compositions of the exsolved phases depart from the solvus at about 480 °C and 530 °C, and the preserved compositions are $a_{ab} = 0.12$ and $a_{ab} = 0.15$ for the orthoclase-rich phase and $a_{ab} = 0.97$ and $a_{ab} = 0.96$ for the albite-rich phase, respectively. For cooling path III, the compositions of the exsolved phases start to depart from the solvus at about 580 °C and the compositions that are finally preserved in the exsolved phases are $a_{ab} = 0.22$ and $a_{ab} = 0.93$, respectively. If cooling is faster than path III, then compositional separation becomes successively more inefficient and the binodal compositions are never reached such as for paths IV and V. The compositions finally preserved from cooling along path IV are $a_{ab} = 0.25$ and $a_{ab} = 0.92$. For cooling at 1°C per day (path V), chemical separation is largely suppressed.

During the initial stage of phase separation a lamellar microstructure develops, in which the characteristic dimension of compositional fluctuations remains constant. As soon as the binodal compositions are reached coarsening begins. The coarsening primarily occurs at high temperature. For cooling paths I to IV practically all the coarsening occurs between 700 °C and 675 °C, that is within the first 25 °C of the cooling path (see fig. 10). It must be noted, however, that chemical separation is effective down to lower temperature, so that chemical maturation continues after coarsening has effectively ceased.

DISCUSSION

Evolution of the Mesoperthite

A schematic drawing of the successive stages of mesoperthite formation is shown in figure 11, column I. According to its integrated bulk composition Or26.5Ab71An2.5 sample TA-76-3 entered the coherent solvus close to the crest at about 690 °C and the coherent spinode at about 680 °C. We assume that primary exsolution occurred by spinodal decomposition at or slightly below the coherent spinodal.

Our model qualitatively describes the morphology of the mesoperthite of sample TA-76-3. We infer that lamellar intergrowth is morphologically stable, and the lamellar microstructure is maintained during coarsening (stage II in fig. 11), when the exsolved phases occur at approximately equal modal proportions. The lamellar microstructure of the mesoperthite is reproduced by our numerical modeling only when the interfacial energy is taken as anisotropic. In contrast, spherical precipitates or irregularly curved co-continuous morphologies are obtained, when the interface energy is taken as isotropic (Petrishcheva and Abart, 2009). This suggests that the interfacial energy of the albite-1-orthoclase-1 interfaces was indeed markedly anisotropic during primary exsolution and coarsening, despite the fact that these interfaces are now incoherent.

The initial wavelength of compositional fluctuations obtained in our modeling appears to be largely independent of the cooling rate. This is in line with the theoretical prediction of Hilliard (1970), which suggests a very weak dependence with $\lambda_0 \propto (1/s)^{1/6}$. In contrast, the extent of coarsening appears to be more strongly related to the cooling rate. Our model predicts an increase of the characteristic dimension of the microstructure during coarsening by a factor on the order of 10 for cooling path I and by a factor of about 2 for cooling path II and III (see fig. 12). It is interesting to note that most of the coarsening occurs during the early stages of cooling. The final

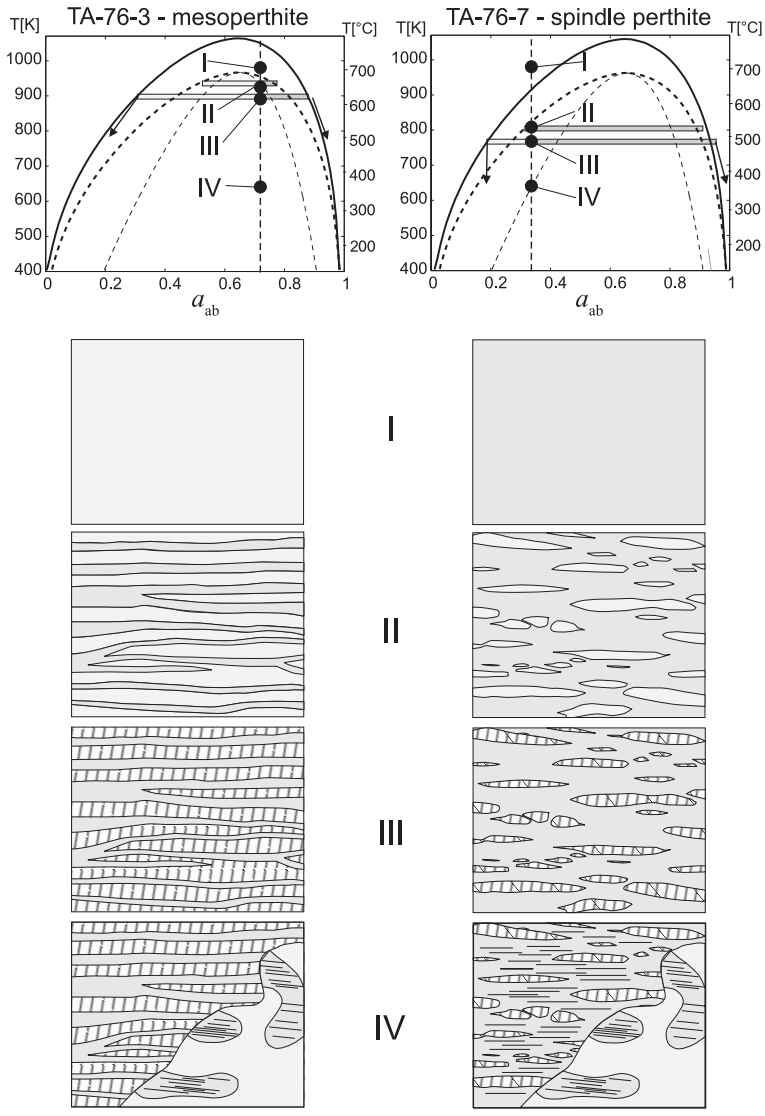

Fig. 11. Schematic $T - a$ diagrams and sketches of the microstructure evolution of the mesoperthite and the spindle perthite from Ngoronghoro; vertical dashed lines in the $T - a$ diagrams indicate bulk compositions of the meso- and spindle perthites, horizontal bars illustrate the modal proportions of the exsolved phases; arrows indicate compositional evolution after the monoclinic to triclinic transformation of the albite-rich phase; (I) homogeneous precursor phase; (II) primary exsolution and coarsening; (III) albite twinning due to monoclinic-triclinic transition of the albite-rich phase; (IV) exsolution of second generation of coherent albite-rich spindles in the orthoclase-rich host of the spindle perthite and replacement by patch perthite during dueteric alteration.

size of the exsolution microstructure is attained after 20 °C of cooling below the coherent solvus for all three cooling paths. To this end, our model confirms the findings of Yund (1984), who suggests a similar relation between cooling rate and lamellar size from application of the experimentally determined growth law of Yund and Davidson (1978). We may infer that the characteristic size of exsolution features reflects the cooling rate during the early stages of the cooling history. The characteris-

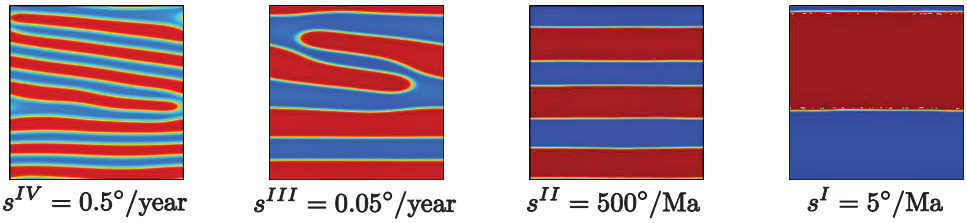

Fig.12. Microstructure preserved in exsolved alkali feldspars of composition $a_{ab} = 0.62$ cooled along paths I to IV; note the increase in lamella width with decreasing cooling rate.

tic spacing of the lamellar microstructure in a mesoperthite may thus be used as a geospeedometer, which reflects cooling rates only for a narrow temperature interval from the temperature of the coherent spinodal at the respective bulk composition to some 20 °C to 30 °C below this temperature. The difference in lamellar size obtained for cooling path I and II is larger than the difference in lamellar size obtained for cooling path II and III (see fig. 12). This suggests that the size of perthite lamellae is a more sensitive monitor for slow cooling rates below 5 °C/Ma than for higher cooling rates. The lamella width on the order of several μm in the mesoperthite from Ngoronghoro indicates that the cooling rate was smaller than about 50 °C/Ma in the temperature interval of 670 °C to 650 °C.

As cooling proceeds chemical separation of the exsolved phases continues down to lower temperatures than does coarsening of the lamellea. The temperature at which the compositions of the exsolved phases depart from the solvus and the compositions that are finally preserved in the exsolved phases depend on cooling rate. The compositions of the exsolved phases may thus be used as geospeedometers as well. In contrast to the characteristic size of the exsolution lamellae, this second geospeedometer reflects cooling rates in the temperature interval between about 480 °C and 580 °C, where the compositional evolution of the exsolved phases departs from the solvus. Due to the asymmetric shape of the solvus, the composition of the orthoclase rich phase is more sensitive to the cooling rate than the composition of the albite-rich phase. The sensitivity of this geospeedometer is higher at high cooling rates than at low cooling rates (see fig. 9). The orthoclase-rich phase of the mesoperthite has a composition of Or90Ab10An0. By comparison with figure 9, this indicates slow cooling at less than 5 °C/Ma in the temperature interval of 480 °C to 530 °C.

As soon as the compositions of the exsolved phases depart from the solvus, they can potentially precipitate feldspars from the opposite limb of the solvus by nucleation and growth. Such a mechanism is more likely to occur along the relatively shallow limb on the orthoclase-rich side of the solvus than on the comparatively steep albite-rich side. Formation of a second generation of fine, albite rich exsolution lamellae in orthoclase-rich domains of coarse mesoperthites has been repeatedly described (Evangelakakis and others, 1993).

Due to its anorthite content of about 3 to 4 mole percent the albite-1 lamellae exsolved with a composition near the peristerite gap. The interfaces between albite-1 and orthoclase-1 lamellae are corrugated, where the structure of the interface correlates with the lamellar peristerite intergrowth within the albite-1 lamellae (see fig. 3F). This is interpreted as a growth phenomenon associated with coarsening of the orthoclase lamellae. It reflects different mobilities of the orthoclase-plagioclase interface in pure albite and more anorthite-rich lamellae of the peristerite intergrowth. The corrugated interface thus testifies to the continued evolution of the microstructure, at least on the sub-micron scale, after albite-1 had exsolved about the peristerite gap.

Evolution of the Spindle Perthite

According to its integrated bulk composition of Or67Ab31.5An1.5, the alkali feldspar of sample TA-76-7 entered the coherent solvus at about 590 °C and the coherent spinode at about 430 °C. It had thus remained in the field of metastability over a temperature range of 160 °C. We assume that given the slow cooling rate in the range of 1 to 10 °C/Ma as inferred from the mesoperthite microstructure (see above), this long period allowed for exsolution by homogeneous nucleation. By analogy with the coherent nature of albite-2 spindles we infer that initially the albite-1 spindles were coherent as well and had similarly high aspect ratio as the albite-2 spindles. We suggest that such thin spindles were morphologically unstable during coarsening and broke up into shorter spindles and blebs, which quickly lost coherency at the phase boundaries. This would then have enhanced chemical separation and allowed the albite-rich precipitates and the orthoclase-rich host to equilibrate along the incoherent solvus during cooling (see fig. 11, column II). For geologically reasonable cooling rates of 1 to 10 °C/Ma, this would allow the spindles and host to equilibrate along the incoherent solvus down to rather low temperature.

Effect of symmetry change and Al-Si ordering in the albite-rich phase.—Equilibration along the solvus during cooling requires exchange of sodium and potassium between the exsolved phases and successive adjustment of the modal proportions as required by mass balance in a closed system. A change in the modal proportions of the exsolved phases and concomitant coarsening require movement of the phase boundaries between the albite-rich and the orthoclase-rich phases. At some stage during cooling, interface migration may, however, be inhibited by the monoclinic to triclinic transformation of the albite-rich phase. Initially the albite-rich phase was metrically and topochemically monoclinic. Due to a displacive phase transformation during cooling the albite-rich phase becomes metrically triclinic (Kroll and others, 1980; Kroll, 1984). This change in symmetry is evident from albite twinning of the albite-1 lamellae and spindles. The monoclinic to triclinic phase transformation also induces Al-Si ordering in the tetrahedral framework, and the albite-rich phase becomes topochemically triclinic on further cooling (Kroll and others, 1980; Kroll, 1984). In contrast, the orthoclase-rich phase remains topochemically monoclinic. If the albite-rich phase is topochemically triclinic and the orthoclase-rich phase is topochemically monoclinic, movement of the albite-orthoclase phase boundaries requires rearrangement of Al- and Si-cations in the tetrahedral framework. This is known to be exceedingly slow as compared to the interdiffusion of the alkali cations (Yund, 1984). This probably hinders further microstructure evolution. This is why we suggest that microstructure evolution stopped, and the modal proportions of the exsolved phases were "frozen in" after the albite-rich precipitates went through the monoclinic to triclinic transformation.

The reduced mobility of the phase boundaries did, however, not hinder the interdiffusion of sodium and potassium cations. During further cooling the albite-rich precipitates and the orthoclase-rich host further separated in composition, albeit in a metastable fashion. Although the detailed trajectory that the exsolved phases may have taken through $T - a$ space cannot be reconstructed, a qualitative statement can be made based on mass balance considerations. Given that the bulk perthites behaved as closed systems, the relative rate at which the less abundant orthoclase-1 lamellae of the mesoperthite of sample Ta-76-3 become successively more potassium rich is about two times the rate at which the albite-1 lamellae become more sodium rich. The compositions of the albite-1 and orthoclase-1 lamellae thus develop sub-parallel to the binodal curve, which is more shallow on the orthoclase-rich limb than on the albite-rich limb (see arrows in fig. 11). In contrast, if phase boundaries become kinetically stranded in the spindle perthite of sample Ta-76-7, the less abundant albite-rich precipitates are

shifted to more sodium rich compositions during cooling, whereas the more abundant orthoclase-rich host hardly changes its composition (see arrows in fig. 11). By this mechanism the orthoclase-rich host may enter the coherent solvus again at a relatively high temperature. The integrated bulk composition of the orthoclase-rich host and the exsolved albite-2 spindles is Or90Ab10An0 indicating that the orthoclase-rich host re-entered the coherent solvus at about 400 °C. We suggest that the coherent albite-2 spindles formed by nucleation and growth at 350 °C to 400 °C. A similar interpretation was given by Evangelakakis and others (1993) for film perthites in slowly cooled perthites from Sri Lanka. The position of the diffuse transformation is well known in the alkali feldspar system (see fig. 1), but the influence of the anorthite content is not well known. For the albite-rich phase of the spindle perthite we infer a temperature of $>$ 480 °C for the diffuse transformation based on the composition of the albite-rich phase. This is also compatible with the modal proportions predicted for the albite- and orthoclase-rich phases from the strain free solvus for the bulk composition of the perthite.

It is conceivable that the albite-2 lamellae are topochemically monoclinic although they formed far below the temperature of the monoclinic-triclinic transition. Exsolution supposedly occurred under "dry" conditions so that rearrangement of the Al-Si tetrahedral framework, which was topochemically monoclinic in the orthoclase host, did not occur. The misfit of the two crystal lattices is accommodated by line defects, which occur at the orthoclase albite-2 interfaces in regular intervals (fig. 6).

Deuteric Alteration

Formation of patch perthite.—The formation of patch perthite at a sharp replacement front from primary perthite is a frequently observed phenomenon (Parsons and Lee, 2009). The patch perthite from Ngoronghoro is interpreted as a result of deuteric alteration of the primary perthites. The phases of the patch perthites are devoid of preferred orientation. This suggests that the interfacial energy was isotropic during deuteric alteration. Patch perthite replaced primary perthites at a sharp replacement front. The characteristic grain size and morphology of the patch perthite were coined at this replacement front. In particular, the chemical separation of sodium and potassium must have occurred within the migrating replacement front. The mechanism of phase separation was thus fundamentally different from primary exsolution, where chemical separation occurred within the volume of the initially homogeneous alkali feldspar. The anisotropy of interfacial energy is thus rather a consequence of the crystallization process than a material specific feature. In contrast, the albite-4 spindles in orthoclase-3 of the patch perthite are strictly oriented (see fig. 3E). This exsolution feature was most likely produced by homogeneous nucleation and growth that is by chemical separation in the volume of the initially homogeneous orthoclase-3.

Incoherent phase boundaries as pathways for fluid infiltration.—Matrix plagioclase as well as the albite-rich lamellae or spindles of the first generation (albite-1) show overgrowth of almost pure albite along their grain and phase boundaries (figs. 4 and 5). This is ascribed to fluid infiltration at a late stage. It is interesting to note that in the spindle perthite of sample TA-76-7 a local increase in the water content of albite and orthoclase is associated with this phenomenon. In and around the albite-rich spindles EEL spectra systematically show an OH related pre-peak prior to the onset of the O-K edge. The water signal is, however, absent in areas, which are devoid of albite-1 spindles and which only contain albite-2 spindles. The elevated water content of the alkali feldspar in and around the albite-1 spindles is ascribed to infiltration of an aqueous fluid during late stages of the cooling history. Fluid infiltration only occurred along the incoherent phase boundaries of the albite-1 spindles. In contrast, the coherent interfaces between albite-2 lamellae and the orthoclase-rich host did not

allow for fluid infiltration and remained essentially dry during this late stage infiltration event.

Albite-rich overgrowth and fluid infiltration is also developed around spindles that seem to be isolated in the orthoclase-rich host. This may be due to interconnection of the albite-rich spindles in the third dimension and/or to fluid infiltration along micro cracks, which connect apparently isolated spindles.

The formation of micro- and nano-porosity along incoherent phase boundaries in exsolved alkali feldspar was described by Fitz Gerald and others (2006). The nature of the interphase boundaries that form during exsolution of alkali feldspar is of great importance for the retention and loss of minor elements and (radiogenic) isotopes (Fitz Gerald and others, 2006; Parsons and others, 2009). A series of elements can substitute into alkali feldspar from minor to relatively appreciable amounts. These include Fe^{3+} on the Al site and Ba, Mg, Sr, Mn, Rb, Cs, and NH^{4+} on the alkali site (Smith and Brown, 1988). If substituted into the alkali feldspar structure, these components are relatively immobile. Impurities and minor elements may, however, segregate into grain- and phase boundaries during exsolution (Wirth, 1996; Hiraga and others, 2004; Fitz Gerald and others, 2006). If segregated into phase boundaries, minor elements may be more mobile and easily extractable by fluids or melts.

CONCLUSIONS

Perthite formation during slow cooling may be complex and involve several stages of unmixing and coarsening. Primary exsolution of a homogeneous alkali feldspar during slow cooling may occur by spinodal decomposition, if the composition of the homogeneous precursor phase is close to the position of the thermal maximum of the respective coherent solvus. There the coherent binodal and spinodal curves closely coincide and exsolution by homogeneous nucleation and growth is rather unlikely. For such compositions typically a mesoperthtite microstructure with lamellar morphology develops. The characteristic size of the lamellae reflects cooling rate during the early stages of the exsolution history, that is from the temperature of the coherent solvus at the respective bulk composition to about 20 °C to 30 °C below this temperature. For a cooling rate of 5 °C/Ma the typical lamella width predicted for mesoperthite from numerical modeling is on the order of a few μm. The characteristic lamella width increases with decreasing cooling rate. The compositions of the exsolved orthoclase also depends on the cooling rate, where the sensitivity is higher for relatively high cooling rates of $\geq$ 50 °C/Ma, and the cooling rate in a temperature interval of about 450 °C to 550 °C is reflected.

We suggest that exsolution occurred by spinodal decomposition in the mesoperthite from Ngoronghoro with bulk composition Or26.5Ab71An2.5. From both, the characteristic lamella width and from the composition of the orthoclase-rich phase, we infer slow cooling at $\leq$ 5° C/Ma. This indicates slow cooling of the rocks in the Ngoronghoro structure over the temperature interval between 680 °C and 480 °C. In alkali feldspar of bulk composition Or67Ab31.5An1.5 from the same area, exsolution most likely occurred by a nucleation and growth mechanism. In this case exsolution produced a spindle perthite microstructure with approximately similar characteristic size as the lamellar microstructure of the mesoperthite. Symmetry breaks and Al-Si ordering in the albite-rich phase probably impeded microstructure evolution upon cooling below the monoclinic-triclinic transformation of albite. This led to the evolution of a second generation of coherent albite spindles in the orthoclase-rich host of the spindle perthite. Both the mesoperthite and the spindle perthite are affected by secondary coarsening, chemical alteration, and formation of patch perthite during late stage deuteric alteration. The incoherent phase boundaries between primary exsolution phases provided pathways for fluid migration during deuteric alteration. In contrast the coherent phase boundaries between orthoclase host of the spindle

perthite and second generation albite spindles were closed to fluid migration during deuteric alteration.

ACKNOWLEDGMENTS

This work was funded by the Deutsche Forschungsgemeinschaft, project AB 314/3-1 within the framework of FOR 741. We thank Martin Okrusch and Herbert Bank for providing the samples and Herbert Kroll for stimulating discussion of the subject. We gratefully acknowledge the constructive review of Guilherme Gualda.

References

Appel, P., Möller, A., and Schenk, V., 1998, High-pressure granulite facies metamorphism in the Pan-African belt of eastern Tanzania: *P-T-t* evidence against granulite formation by continent collision: Journal of Metamorphic Geology, v. 16, p. 491–509, doi:10.1111/j.1525-1314.1998.00150.x.

Altherr, R., Okrusch, M., and Bank, H., 1982, Corundum- and kyanite-bearing anatexites from the Precambrian of Tanzania: Lithos, v. 15, p. 191–197, doi:10.1016/0024-4937(82)90010-X.

Brady, J. B., 1983, Intergranular diffusion in metamorphic rocks: American Journal of Science, v. 283-A, p. 181–200.

Brown, W. L., and Parsons, I., 1984, Exsolution and coarsening mechanisms and kinetics in an ordered cryptoperthite series: Contributions to Mineralogy and Petrology, v. 86, p. 3–18, doi:10.1007/BF00373706.

——— 1988, Zoned ternary feldspars in the Klokken intrusion: exsolution microtextures and mechanisms: Contributions to Mineralogy and Petrology, v. 98, p. 444–454, doi:10.1007/BF00372364.

Cahn, J. W., 1962, Coherent fluctuations and nucleation in isotropic solids: Acta Metallurgica, v. 10, p. 907–913, doi:10.1016/0001-6160(62)90140-2.

——— 1968, Spinodal decomposition: Transactions of the Metallurgical Society of AIME, v. 242, p. 166–180.

Cahn, J. W., and Hilliard, J. E., 1958, Free energy of a Nonuniform System. I. Interfacial free energy: Journal of Chemical Physics, v. 28, p. 258–267, doi:10.1063/1.1744102.

Champness, P., and Lorimer, G., 1976, Exsolution in Silicates, *in* Wenk, H. R., editor, Electron Microscopy in Mineralogy: Berlin, Springer Verlag. p. 174–204.

Christoffersen, R., and Schedl, A., 1980, Microstructure and thermal history of cryptoperthites in a dike from Big Bend, Texas: American Mineralogist, v. 65, p. 444–448.

Day, H. W., and Brown, V. M., 1980, Evolution of Perthite Composition and Microstructure During Progressive Metamorphism of Hypersolvus Granite, Rhode Island, USA: Contributions to Mineralogy and Petrology, v. 72, p. 353–365, doi:10.1007/BF00371344.

Evangelakakis, C., Kroll, H., Voll, G., Wenk, H.-R., Hu, M., and Köpcke, J., 1993, Low-temperature coherent exsolution in alkali feldspars from high-grade metamorphic rocks of Sri-Lanka: Contributions to Mineralogy and Petrology, v. 114, p. 519–532, doi:10.1007/BF00321756.

Fitz Gerald, J. D., Parsons, I., and Cayzer, N., 2006, Nannotunnels and pull-aparts: Defects of exsolution lamellae in alkali feldspars: American Mineralogist, v. 91, p. 772–783, doi:10.2138/am.2006.2029.

Foland, K., 1974, Alkali diffusion in orthoclase, *in* Hoffman, A. W., Giletti, B. J., Yoder, H. S., Jr., and Yund, R. A., editors, Geochemical Transport and Kinetics: Washington, Academic Press, Carnegie Institution of Washington Publication 634, p. 77–98.

Grove, T., 1982, Use of exsolution lamellae in lunar clinopyroxenes as cooling rate speedometers—an experimental calibration: American Mineralogist, v. 67, p. 251–268.

Hilliard, J. E., 1970, Spinodal Decomposition, *in* Aaronson, H. F., editor, Phase Transformations: Metals Park, Ohio, American Society of Metals, p. 497–560.

Hiraga, T., Anderson, I. M., and Kohlstedt, D. L., 2004, Grain boundaries as reservoirs of incompatible elements in the Earth's mantle: Nature, v. 427, p. 699–703, doi:10.1038/nature02259.

Hovis, G. L., Delbove, F., and Bose, M. R., 1991, Gibbs energies and entropies of K-Na mixing for alkali feldspar from phase equilibrium data: implications for feldspar solvi and short range order: American Mineralogist, v. 76, p. 913–927.

Hovis, G. L., Kroll, H., Breit, U., and Yund, R. A., 2003, Elastic strain enthalpies of exsolution: HF solution calorimetric experiments on alkali aluminosilicate and aluminogermanate feldspars: American Mineralogist, v. 88, p. 547–555.

Kasper, R., ms, 1975, Cation and oxygen diffusion in albite: Providence, Rhode Island, Brown University, Ph. D. thesis.

Kay, S. M., 1977, The origin of antiperthites in anorthosites: American Mineralogist, v. 62, p. 905–912.

Kroll, H., 1984, Thermal expansion of alkali feldspars, *in* Brown, W. L., editor, Feldspars and Feldspathoids: NATO ASI, v. C137, p. 163–205.

Kroll, H., Bambauer, H. U., and Schirmer, U., 1980, The high albite-monalbite and the analbite-monalbite transitions: American Mineralogist, v. 65, p. 1192–1211.

Kuhl, E., and Schmid, D. W., 2007, Computational modeling of mineral unmixing and growth: Computational Mechanics, v. 39, p. 439–451, doi:10.1007/s00466-006-0041-1.

Maboko, M. A. H., Boelrijk, N. A. I. M., Priem, H. N. A., and Verdurinen, E. A. Th., 1985, Zircon U-Pb and biotite Rb-Sr dating of the Wami River granulites, Eastern Granulites, Tanzania: Evidence for approximately 715 Ma old granulite-facies metamorphism and final Pan-African cooling approximately 475 Ma ago: Precambrian Research, v. 30, p. 361–378, doi:10.1016/0301-9268(85)90088-9.

McCallister, R. H., and Yund, R. A., 1977, Coherent exsolution in Fe-free pyroxenes: American Mineralogist, v. 62, p. 721–726.
Meert, J. G., van der Voo, R., and Ayub, S., 1995, Paleomagnetic investigation of the Neoproterozoic Gagwe lavas and Mbozi complex, Tanzania and the assembly of Gondwana: Precambrian Research, v. 74, p. 225–244, doi:10.1016/0301-9268(95)00012-T.
Menna, M., Tribaudino, M., and Renzulli, A., 2008, Al-Si order and spinodal decomposition texture of a sanidine from igneous clasts of Stromboli (southern Italy): insights into the timing between the emplacement of a shallow basic sheet intrusion and the eruption of related ejecta: European Journal of Mineralogy, v. 20, p. 183–190, doi:10.1127/0935-1221/2008/0020-1795.
Nauman, E. B., and He, D. Q., 2001, Nonlinear diffusion and phase separation: Chemical Engineering Science, v. 56, p. 1999–2018, doi:10.1016/S0009-2509(01)00005-7.
Owen, D. C., and Mc Connell, J. D. C., 1974, Spinodal unmixing in an alkali feldspar, *in* MacKenzie, W. S., and Zussman, J., editors, The Feldspars: Manchester, England, Manchester University Press, p. 424–439.
Parsons, I., 1978, Feldspars and fluids in cooling plutons: Mineralogical Magazine, v. 42, p. 1–17, doi:10.1180/minmag.1978.042.321.01.
Parsons, I., and Brown, W. L., 1983, A TEM and Microprobe Study of a Two-perthite Alkali Gabbro: Implications for the Ternary Feldspar System: Contributions to Mineralogy and Petrology, v. 82, p. 1–12, doi:10.1007/BF00371170.
Parsons, I., and Lee, M. R., 2009, Mutual replacement reactions in alkali feldspars I: microtextures and mechanisms: Contributions to Mineralogy and Petrology, v. 157, p. 641–661, doi 10.1007/s00410-008-0355-4.
Parsons, I., Thompson, P., Lee, M. R., and Cayzer, N., 2005, Alkali feldspar microtextures as provenance indicators in siliciclastic rocks and their role in feldspar dissolution during transport and diagenesis: Journal of Sedimentary Research, v. 75, p. 921–942, doi:10.2110/jsr.2005.071.
Parsons, I., Magee, C. W., Allen, C. M., Shelley, J. M. G., and Lee, M. R., 2009, Mutual replacement reactions in alkali feldspars II: trace element partitioning and geothermometry: Contributions to Mineralogy and Petrology, v. 157, p. 663–687, doi 10.1007/s00410-008-0358-1.
Petrishcheva, E., and Abart, R., 2009, Exsolution by spinodal decomposition I: Evolution equation for binary mineral solutions with anisotropic interfacial energy: American Journal of Science, v. 309, p. 431–449, doi 10.2475/06.2009.01.
Robin, P., 1974, Stress and strain in cryptoperthite lamellae and the coherent solvus of alkali feldspar: American Mineralogist, v. 59, p. 1299–1318.
Shimizu, I., and Takei, Y., 2005, Thermodynamics of interfacial energy in binary metallic systems: influence of adsorption on dihedral angles: Acta Materialia, v. 53, p. 811–821, doi:10.1016/j.actamat.2004.10.033.
Smith, J. V., and Brown, W., 1988, Feldspar Minerals, Volume 1: Crystal Structures, Physical, Chemical, and Microtextural Properties: Berlin, Springer Verlag, 828 p.
Wirth, R., 1996, Thin amorphous films (1-2 nm) at olivine grain boundaries in mantle xenoliths from San Carlos, Arizona: Contributions to Mineralogy and Petrology, v. 124, p. 44–54.
——— 2004, Focused ion beam (FIB): A novel technology for advanced application of micro- and nanaoanalysis in geosciences and applied mineralogy: European Journal of Mineralogy, v. 16, p. 863–876, doi:10.1007/s004100050172.
Yund, R., 1984, Alkali Feldspar exsolution: Kinetics and dependence on alkali interdiffusion, *in* Brown, W. L., editor, Feldspars and feldspathoids: Structure, Properties, and Occurrences: Dordrecht, D. Reidel Publishing Company, NATO Advanced Science Institute Series C, v. 137, p. 281–315.
Yund, R. A., and Ackermand, D., 1979, Development of Perthite Microstructures in the Storm King Granite, N.Y.: Contributions to Mineralogy and Petrology, v. 70, p. 273–280, doi:10.1007/BF00375357.
Yund, R. A., and Chapple, W. M., 1980, Thermal histories of two lava flows estimated from cryptoperthite lamellar spacings: American Mineralogist, v. 65, p. 438–443.
Yund, R. A., and Davidson, P., 1978, Kinetics of lamellar coarsening in cryptoperthites: American Mineralogist, v. 63, p. 470–477.
Yund, R., and Tullis, J., 1983, Subsolidus phase relations in the alkali feldspars with emphasis on coherent phases, *in* Ribbe, P. H., editor, Feldspar Mineralogy: Mineralogical Society of America, Reviews in Mineralogy, p. 141–176.
Yund, R., Ackermand, D., and Seifert, F., 1980, Microstructures in the alkali feldspars from the granulite complex of Finnish Lapland: Neues Jahrbuch für Mineralogie Monatshefte, v. 3, p. 109–117.
Yund, R. A., McLaren, A. C., and Hobbs, B. E., 1974, Coarsening kinetics of the exsolution microstructure in alkali feldspar: Contributions to Mineralogy and Petrology, v. 48, p. 45–55, doi:10.1007/BF00399109.